# Strain-Tunable Electronic and Optical Properties of Lead-Free Halide Perovskite $Ca_3PBr_3$: A First-Principles Study

**Fatemeh Nemati*[,1], Reza Habibpourbisafar[2], Elaheh Javanshoor[1]**

[1]**Department of Physics, Urmia University of Technology, Urmia, Iran**

[2]**Department of Physics, Faculty of Science, University of Tabriz, Tabriz, Iran**

*fateme.nemati@sci.uut.ac.ir

**Abstract**

The global pursuit of sustainable and non-toxic materials for optoelectronic applications has directed increasing attention toward lead-free halide perovskites. In this study, the structural, electronic, optical, and mechanical properties of $Ca_3PBr_3$ were systematically investigated using first-principles calculations based on density functional theory (DFT). Both the generalized gradient approximation (GGA-PBE) and the hybrid HSE06 exchange-correlation functional were employed, with spin–orbit coupling (SOC) incorporated to capture relativistic effects. The results reveal that $Ca_3PBr_3$ possesses a direct bandgap of 1.64 eV (GGA) and 2.47 eV (HSE06), which can be efficiently tuned within a range of 0.38 eV under biaxial strain from -4% to +4%. The projected density of states (PDOS) indicates that the valence band is primarily derived from Br-4p and P-3p orbitals, while Ca-3d states dominate the conduction band. Optical analyses show strong light absorption in the visible range, with strain-dependent modulation of the absorption edge, refractive index, and dielectric function. Mechanical stability tests confirm that $Ca_3PBr_3$ satisfies the Born criteria under all applied strain conditions, maintaining robust structural integrity. These findings identify $Ca_3PBr_3$ as a mechanically stable, environmentally benign, and strain-tunable semiconductor suitable for next-generation flexible optoelectronic, piezoelectric, and spintronic devices.

**Keyword:** Lead-free perovskite, strain engineering, spin-orbit coupling, optoelectronics, First-principles calculations.

## 1. Introduction

The remarkable progress of halide perovskite materials has profoundly transformed the landscape of optoelectronics, with particularly significant advances in photovoltaics and photodetection [1, 2]. Their unique attributes, including large absorption coefficients, tunable bandgaps, long carrier diffusion lengths, and low exciton binding energies, position them as compelling alternatives to traditional semiconductors such as silicon and GaAs [3]. Nevertheless, the intrinsic toxicity and instability of lead-based perovskites have driven global research efforts toward designing lead-free halide perovskites with comparable, or even superior, optoelectronic performance [4, 5].

Concurrently, the rapid reduction in the manufacturing costs of crystalline silicon solar cells has accelerated the large-scale adoption of photovoltaic (PV) technology. Forecasts suggest that by 2030, solar power may account for nearly one-third of newly installed global electricity capacity [3]. While high-purity crystalline silicon has already achieved power conversion efficiencies (PCEs) exceeding 26% alongside excellent long-term stability[6, 7], emerging thin-film PV technologies-typically less than 1μm in thickness-offer additional advantages, such as cost-effectiveness and ease of integration with flexible substrates. Within this context, lead halide perovskite solar cells (PSCs) have emerged as frontrunners, achieving PCEs above 22% by 2016 and rivaling established technologies such as Si, CdTe, and GaAs [4]. These compounds generally adopt the $ABX_3$ crystal structure, where organic (MA, FA) or inorganic (Cs, Rb) cations occupy the A-site, Pb resides at the B-site, and halides ($I^-$, $Br^-$, $Cl^-$) populate the X-sites[4].

Beyond photovoltaics, halide perovskites have also demonstrated broad applicability in optoelectronic devices such as light-emitting diodes (LEDs), lasers, photodetectors, and radiation sensors, owing to their bandgap tunability, strong photoluminescence, and defect tolerance [8]. Hybrid organic--inorganic perovskites, notably $MAPbI_3$ and $FAPbI_3$, have achieved PCEs exceeding 25%, competing directly with crystalline silicon [3]. However, their susceptibility to degradation under moisture, oxygen, and thermal stress, together with the environmental hazards posed by Pb-based compounds, continues to hinder their commercial deployment at scale [4].

To overcome these limitations, several material strategies have been proposed. These include (i) all-inorganic perovskites (e.g., $CsPbX_3$), which offer improved thermal stability; (ii) double perovskites such as $Cs_2AgBiBr_6$, in which $Pb^{2+}$ is replaced by benign cations [9]; and (iii) entirely new classes of lead-free perovskites based on alkaline-earth or transition-metal cations (Ca, Sr, Sn, Ge), which maintain the perovskite framework while eliminating toxicity. Among these, Sn-based compounds such as $MASnI_3$ have been investigated as Pb analogues, but their stability is undermined by the facile oxidation of $Sn^{2+}$ to $Sn^{4+}$ [4]. Consequently, alkaline-earth-based halide perovskites (e.g., Ca- and Sr-containing systems) have recently emerged as promising candidates, offering favorable band structures, structural robustness, and environmental safety. Recent reviews further highlight progress in lead-free halide perovskites for stable and eco-friendly optoelectronics [10].

Recent computational and experimental studies have expanded the family of lead-free halide perovskites to include Ca-, Sr-, and Ba-based compounds exhibiting excellent structural stability and tunable electronic properties under strain and composition modulation [11]. Previous theoretical studies have investigated $Ca_3PBr_3$ using first-principles DFT calculations, reporting its structural stability, direct bandgap, elastic constants, and optical properties, and have further assessed its photovoltaic potential through device-level SCAPS-1D modeling [12, 13]. Despite these efforts, research specifically focused on $Ca_3PBr_3$ remains limited. More broadly, first-principles studies on Ca-based and alkaline-earth halide perovskites have demonstrated favorable structural stability and electronic characteristics, highlighting their promise as environmentally benign alternatives to Pb-based systems [11, 14, 15]. In particular, DFT investigations have shown that Ca-containing halide perovskites can exhibit direct bandgaps and strong optical absorption suitable for optoelectronic applications [11, 16]. However, these studies have largely been restricted to equilibrium conditions, leaving the influence of external mechanical strain on the electronic and optical properties of $Ca_3PBr_3$ insufficiently explored.

The key novelty of this work lies in the first comprehensive investigation of biaxial strain and spin–orbit coupling effects on the electronic, optical, and mechanical properties of $Ca_3PBr_3$—a hypothetical yet promising lead-free halide perovskite. Strain engineering has emerged as an effective strategy for tuning the electronic structure and optical response of halide perovskites. Both experimental and theoretical studies on Pb-based and double perovskite systems, such as $MAPbI_3$, $CsPbBr_3$, and $Cs_2AgBiBr_6$, have shown that biaxial strain can induce significant bandgap modulation while preserving structural stability [9, 15, 17]. Comparable strain-induced trends have also been reported for alkaline-earth halide perovskites, indicating that mechanical deformation plays a crucial role in tailoring their optoelectronic behavior [14]. Nevertheless, a systematic strain-dependent investigation of $Ca_3PBr_3$ is still lacking.

In addition, spin–orbit coupling is known to be essential for accurately describing the electronic band structure and optical properties of halide perovskites containing heavy halogens such as bromine. Previous studies have demonstrated that SOC leads to bandgap narrowing, modifies band-edge dispersion, and enhances dielectric screening in both hybrid and inorganic perovskites [18]. Despite its recognized importance, the combined effects of biaxial strain and SOC on $Ca_3PBr_3$ have not yet been reported. In this work, we address these gaps by presenting a comprehensive first-principles investigation of the structural, electronic, optical, and mechanical properties of $Ca_3PBr_3$ under biaxial strain. By explicitly incorporating SOC and evaluating mechanical stability through elastic constants and Born stability criteria [19] ,this study provides a unified understanding of strain-driven optoelectronic tunability in a lead-free halide perovskite. The key novelties of the present work lie in the combined analysis of biaxial strain, spin–orbit coupling, and mechanical stability within a single first-principles framework, extending beyond previous equilibrium and device-level studies.

## 2. Computational details

In this work, we investigated the structural and electronic properties of the ternary halide perovskite $Ca_3PBr_3$ using first-principles calculations as implemented in QuantumATK (version 2020 [20]. The study was grounded in Density Functional Theory (DFT) to obtain accurate insights into the atomic and electronic configurations of the system. Full geometry optimization was carried out to minimize internal stresses and achieve the ground-state configuration (e.g. following computational protocols in ref [21]. The atomic con

uration was fully optimized using the Limited-memory Broyden–Fletcher–Goldfarb–Shanno (LBFGS) algorithm [22], with convergence thresholds of 0.05 eV/Å for atomic forces and $10^{-6}$ eV for total energy. Geometry optimization was performed in a fully variable cell scheme, allowing both atomic positions and lattice vectors to relax until the residual stress on the simulation cell fell below 0.001 GPa. The Linear Combination of Atomic Orbitals (LCAO) method was employed for wavefunction representation. A Double-Zeta Polarized (DZP) basis was used with norm-conserving pseudopotentials; exchange–correlation was treated within GGA using the PBE functional [23]. For band-gap benchmarking we also employed the HSE06 hybrid functional [24, 25]. The Brillouin zone was sampled using a 7×7×7 Monkhorst–Pack mesh [26]. SOC was incorporated within the PBE framework using norm-conserving pseudopotentials from the SOGGA basis set. Due to computational constraints, self-consistent SOC calculations with the HSE06 hybrid functional were not feasible. The HSE06 results provide accurate bandgaps, while SOGGA-PBE exchange-correlation functional quantifies the relativistic correction, following established methods for heavy-halide perovskites.

In this study, biaxial strain is applied uniformly in the X–Y plane of the $Ca_3PBr_3$ unit cell, while the lattice parameter along the Z axis is allowed to fully relax to minimize the total energy. Compressive and tensile strain are defined by varying the in-plane lattice constants simultaneously, and this strain configuration is adopted consistently for all electronic, optical, and mechanical calculations presented throughout the manuscript.

## 3. Results and discussion

### 3.1. Structural Properties

The crystal structure of $Ca_3PBr_3$ was modeled based on the cubic perovskite framework with space group $P\bar{m}3m$ (No. 221) (See Fig.1). In this configuration, calcium ($Ca^{2+}$) occupies the A-site at Wyckoff position 3c (0, 0.5, 0.5), phosphorus ($P^{3-}$) resides at the B-site at position 1b (0.5, 0.5, 0.5), and bromine ($Br^{-}$) completes the octahedral coordination at position 3d (0.5, 0, 0). The optimized lattice constant for cubic $Ca_3PBr_3$ is a = 6.45 Å, corresponding to a unit-cell volume of 268.3 $Å^3$. The calculated P–Br bond length is 2.31 Å and the Ca–Br distance is 2.86 Å, with the Br–P–Br bond angle fixed at $90^\circ$ by symmetry. These values are consistent with the typical bond lengths observed in halide perovskites. Table 1 compares our calculated lattice constants with those from previous theoretical studies. Our DFT calculations yield a relaxed lattice constant for $Ca_3PBr_3$ in excellent agreement with previously reported DFT results, while the slightly smaller value obtained with HSE06 (6.42 Å) reflects the tendency of hybrid functionals to predict shorter bonds. Also, the Energy Volume curve of $Ca_3PBr_3$ is added (see Fig.2).

### 3.2. Mechanical properties

The elastic constants of crystalline solids provide fundamental insight into their mechanical behavior and stability. For a cubic system, mechanical stability is governed by the Born stability criteria [19]. As shown in Table 2, all calculated elastic constants of $Ca_3PBr_3$ satisfy these criteria under the entire range of applied biaxial strain, namely $C_{11} > 0$, $C_{44} > 0$, $C_{11} > C_{12}$ and $C_{11} + 2C_{12} > 0$, $C_{11} - C_{12} > 0$ confirming the mechanical stability of the material (Born-Huang stability criteria). With increasing tensile strain, the elastic constant $C_{11}$ and the Pugh ratio($B/G$) exhibit a pronounced decrease, indicating a gradual softening of the lattice. Such behavior is characteristic of halide perovskites, where tensile deformation weakens interatomic interactions and reduces resistance to volume-preserving deformation [15]. Similarly, the shear modulus-related quantity $C_{44}$ decreases monotonically under tensile strain, reflecting a reduced resistance to shear stress and an enhanced tendency toward ductile mechanical behavior. The consistently negative values of the Cauchy pressure ($C_{12}$-$C_{44}$) across all strain states suggest the presence of directional bonding contributions to the mechanical response, a feature previously reported for lead-based perovskites such as $MAPbI_3$ and $CsPbBr_3$ [17]. In comparison with these Pb-containing systems, $Ca_3PBr_3$ exhibits comparable bulk-to-shear modulus ratios while benefiting from the absence of toxic lead, making it a more environmentally benign alternative. The strain-induced softening observed here is also consistent with trends reported for double perovskites such as $Cs_2AgBiBr_6$, where tensile strain reduces lattice stiffness and enhances ductility, whereas compressive strain increases rigidity [9]. Importantly, even at the maximum applied tensile strain of +4% all elastic constants of $Ca_3PBr_3$ remain positive and satisfy the mechanical stability criteria, underscoring its suitability for applications in flexible and strain-tolerant optoelectronic devices.

## 3.3. Electronic Structure and Bandgap Engineering

The band structure of $Ca_3PBr_3$, calculated along high-symmetry directions in the Brillouin zone, reveals a direct bandgap, confirming its semiconducting character (See Table 3 for more details.). Using the GGA-PBE functional, the unstrained bandgap is 1.6395 eV, while the HSE06 hybrid functional yields a value of 2.4722 eV (see Fig. 3(a)), in line with previous theoretical studies [12, 13]. The GGA-PBE functional is widely used due to its computational efficiency and reliability in structural optimization, but it is known to underestimate semiconductor band gaps because of self-interaction errors and the lack of derivative discontinuity in the exchange-correlation potential. In contrast, the HSE06 hybrid functional includes a fraction of screened exact exchange, providing a more accurate description of band-edge states and yielding band-gap values closer to experimental measurements. Therefore, a common and practical approach is to optimize the structure using GGA-PBE and evaluate electronic properties with HSE06, which is confirmed by [12]. The direct bandgap and strong optical absorption make $Ca_3PBr_3$ attractive for optoelectronic applications.

To improve accuracy, spin–orbit coupling was incorporated using SOGGA-PBE exchange-correlation functional [18]. Including SOC via the SOGGA-PBE exchange-correlation functional set narrows the bandgap to 1.6173 eV (Fig. 3 (b)), reflecting the influence of relativistic effects in bromine-containing perovskites. These findings highlight the necessity of including SOC for reliable electronic property predictions in halide perovskites. According to the Shockley-Queisser detailed-balance limit, the optimal band gap for single-junction solar cells lies in the range of approximately 1.3-1.4 eV, while materials with band gaps between about 1.1 and 1.6 eV can still achieve high theoretical efficiencies depending on device architecture and loss mechanisms [3, 27]. Like high-performing perovskite solar cells, materials in this category can effectively absorb the visible spectrum and transform sunlight into electrical power.

## 3.4. Strain-Tunable Electronic Properties

Biaxial strain engineering reveals a pronounced tunability of the electronic bandgap in $Ca_3PBr_3$. Under compressive strain (-4%), the bandgap decreases to 1.4604 eV within GGA-PBE exchange-correlation functional and 1.4372 eV using SOGGA-PBE functionals, whereas tensile strain (+4%) leads to a widening of the bandgap to 1.8366 eV (GGA-PBE exchange-correlation functional) and 1.8176 eV (SOGGA-PBE exchange-correlation functional) (Fig. 4). This reversible, monotonic modulation of the bandgap with strain is a hallmark of straintronics and is crucial for the design of flexible, adaptive optoelectronic devices. In all cases, inclusion of SOC consistently results in a slightly lower bandgap compared to GGA alone.

Comparable strain-induced trends have been reported for other halide perovskites. For example, Jiang et al. demonstrated in $MAPbI_3$ that biaxial strain of ±3% tunes the bandgap by nearly 0.3 eV, with compressive strain causing a redshift and tensile strain a blueshift [15]. Similarly, Islam et al. reported that the bandgap of $CsPbBr_3$ narrows under compressive strain and widens under tensile strain, consistent with our observations for $Ca_3PBr_3$ [17]. Even in double perovskites such as $Cs_2AgBiBr_6$, theoretical studies find that biaxial strain can tune the bandgap within a 0.2–0.4 eV window while preserving structural stability [9]. The calculated tuning range of 0.38 eV (from 1.46 eV to 1.84 eV) is therefore in good agreement with these earlier reports, confirming the universal strain sensitivity of halide perovskite band structures. A similar monotonic dependence of bandgap energy on biaxial strain has also been reported in recent studies of inorganic halide systems, confirming the generality of strain-driven band-edge modulation in perovskite-related materials [28]. The strain-tunable band gap of $Ca_3PBr_3$ is particularly attractive for integration in tandem solar cells because band-gap matching between sub-cells is a key requirement for maximizing overall power-conversion efficiency [4]. In tandem architectures, materials with different band gaps are stacked to efficiently harvest different portions of the solar spectrum, and the ability to tune the band gap of $Ca_3PBr_3$ via strain enables optimization of its absorption edge to complement commonly used bottom-cell absorbers such as crystalline silicon. This flexibility facilitates improved current matching between sub-cells and enhances the efficiency potential of tandem photovoltaic devices. Moreover, being lead-free, $Ca_3PBr_3$ addresses the toxicity and environmental concerns associated with traditional Pb-based perovskite solar cells. The solar cell industry is actively seeking such alternatives to meet regulatory and sustainability requirements.

### 3.5. Projected Density of States (PDOS) and Orbital Contributions

The projected density of states analysis indicates that the valence band maximum of $Ca_3PBr_3$ is predominantly composed of Br-4p and P-3p orbitals, whereas the conduction band minimum is dominated by Ca-3d states. This orbital separation between the halogen–phosphorus *p* states at the valence edge and alkaline-earth *d* states at the conduction edge is consistent with the electronic structure of many halide perovskites, where the frontier bands typically derive from anion *p* orbitals and metal cation *d* orbitals [18]. The inclusion of spin–orbit coupling introduces slight band-edge shifts, narrowing the bandgap and modifying the density of states near the conduction edge, in line with prior reports that relativistic effects are particularly significant in Br- and I-containing perovskites [18, 29].

Importantly, under applied biaxial strain, the orbital character of both valence and conduction states remains unchanged, but the relative positions of the band edges shift, confirming that strain affects the electronic bandgap without altering the fundamental orbital composition. Similar observations have been reported in lead-halide perovskites: for example, Islam et al. found that in $CsPbBr_3$ the Pb-6p orbitals dominate the conduction edge while halogen *p* orbitals form the valence band, with strain primarily modulating the relative orbital overlap and band dispersion rather than changing orbital identity [17]. In double perovskites such as $Cs_2AgBiBr_6$, Zhou et al. likewise reported that Br-4p states control the valence edge, while Bi-6p and Ag-d states shape the conduction band, and that strain-induced shifts occur without changing orbital dominance [9].

Figure.5 presents the PDOS of $Ca_3PBr_3$ under -4%, -2%, +2%, and +4% biaxial strain, computed using both GGA-PBE and SOGGA-PBE exchange-correlation functionals. In all cases, the valence band is dominated by Br-4p and P-3p orbitals, while the conduction band consists mainly of Ca-3d states, are in line with the unstrained case. Under compressive strain, the valence- and conduction-band edges shift closer together, leading to a narrowed bandgap, whereas tensile strain produces the opposite effect, widening the gap. Inclusion of SOC systematically shifts the conduction-band edge downward, slightly reducing the bandgap. Importantly, the orbital characters remain invariant, indicating that strain modulates the bandgap primarily through changes in orbital overlap and bond lengths rather than altering the fundamental orbital composition. These findings align closely with earlier theoretical and experimental observations on halide perovskites. For instance, Filip et al. reported that the valence edge of $APbX_3$ compounds is dominated by halogen *p* states while the conduction edge arises from Pb *p* orbitals, and that the inclusion of SOC significantly refines band-edge positions [8]. Similarly, Even et al. demonstrated that SOC narrows the bandgap in $MAPbI_3$ by shifting the conduction edge, emphasizing the importance of relativistic corrections in heavy-halide systems [18]. More recent strain studies on $CsPbBr_3$ have shown that compressive strain induces a redshift and tensile strain a blueshift in optical absorption spectra, without altering the orbital makeup of the frontier bands [17]. In double perovskites such as $Cs_2AgBiBr_6$, Zhou et al. found that the Br-4p states consistently form the valence edge and Bi/Ag-derived states dominate the conduction edge, with strain tuning the bandgap magnitude while leaving orbital character intact [9].

### 3.6. Optical Properties

The strain-dependent optical response of $Ca_3PBr_3$ is fundamentally governed by the modulation of its electronic band structure. As established in Section~3.1, biaxial strain systematically tunes the bandgap($E_g$): compressive strain narrows $E_g$ by increasing orbital overlap and reducing bond lengths, while tensile strain widens $E_g$ by decreasing orbital interaction and elongating bonds. This bandgap change directly dictates the energy of interband optical transitions. Consequently, the imaginary part of the dielectric function, $\varepsilon_2(\omega)$, which describes optical absorption, exhibits a redshift in its onset under compression and a blueshift under tension. Physically, the redshift under compression reflects increased orbital overlap and reduced bond lengths that lower transition energies, while the blueshift under tension arises from decreased orbital interaction and elongated bonds. These strain-induced shifts in $\varepsilon_2(\omega)$ directly cause corresponding changes in $\varepsilon_1(\omega)$ via the

Kramers-Kronig transform, which relates absorption to dispersion, and propagate to all derived optical constants. Since all optical properties are derived from the complex dielectric function $\varepsilon(\omega) = \varepsilon_1(\omega) + i\varepsilon_2(\omega)$, we first discuss its strain-dependent behavior.

Figure. 6 confirms this physical picture. The GGA-PBE results show a clear redshift/blueshift of dielectric peaks with compression/tension, aligning with trends in other halide perovskites[15, 17]. The HSE06 functional provides sharper, more accurate band-edge features, while SOC inclusion (SOGGA-PBE exchange-correlation functionals) redshifts the spectra due to bandgap narrowing and enhances low-energy dielectric screening, consistent with behavior in $MAPbI_3$ [18]. The energy loss function ($L(\omega)$) (Fig. 7) defined from $\varepsilon(\omega)$, reveals collective plasmonic excitations. Its dominant peak near 5 eV shifts with strain—redshifting under compression and blueshifting under tension—due to changes in the plasma frequency linked to the altered band structure. SOC refines this response, lowering peak energies and revealing finer spectral details [18]. As shown in Fig. 8, all derived optical coefficients follow the fundamental strain–bandgap relationship:

**Absorption coefficient:** The onset shifts by ~0.4 eV, enabling strain-tunable spectral responsivity.

**Reflectivity:** Peaks shift accordingly, modifying the surface optical response.

**Extinction coefficient:** Intensity increases under compression due to stronger interband transitions.

**Refractive index:** The static value $n(0)$ rises under compression. This trend physically corresponds to enhanced electronic polarizability when the bandgap narrows, as lower transition energies allow easier displacement of charge. The extinction coefficient, directly related to absorption strength, shows intensified low-energy features under compression where transition matrix elements increase due to stronger orbital hybridization.

These trends confirm $Ca_3PBr_3$ follows the characteristic strain-optics relationship of halide perovskites [9, 15, 17]. The optical conductivity $\sigma(\omega)$ (Fig. 9)integrates these effects, showing clear shifts in interband transition thresholds with strain. The consistent, physically-grounded modulation across all optical properties demonstrates $Ca_3PBr_3$'s strong potential for strain-engineered optoelectronic devices.

## 4. Conclusion

This first-principles investigation comprehensively demonstrates that $Ca_3PBr_3$ is a promising lead-free halide perovskite with highly tunable electronic and optical properties, coupled with robust mechanical stability under biaxial strain. Our calculations reveal a direct bandgap of 1.64 eV (GGA-PBE) and 2.47 eV (HSE06) at equilibrium, which can be monotonically modulated by 0.38 eV under biaxial strain ranging from –4% to +4%. The inclusion of SOC further refines the band structure, inducing a consistent redshift in the bandgap due to relativistic effects associated with bromine.

Mechanically, $Ca_3PBr_3$ satisfies the Born stability criteria across all strain levels, confirming its structural integrity under deformation. The elastic constants decrease systematically with increasing tensile strain, indicating lattice softening and enhanced ductility—a desirable trait for flexible device integration. The negative Cauchy pressure across all strain states suggests a contribution from directional covalent bonding, similar to Pb-based perovskites, yet without the associated toxicity.

Electronically, the projected density of states confirms that the valence band maximum is dominated by Br-4p and P-3p states, while the conduction band minimum is primarily composed of Ca-3d states. This orbital composition remains unchanged under strain, confirming that bandgap tuning arises from shifts in band edge positions rather than alterations in orbital character. The system maintains a direct bandgap throughout the applied strain range, preserving its semiconducting nature.

Optically, $Ca_3PBr_3$ exhibits strong absorption in the visible spectrum, with the absorption edge shifting predictably with strain: compressive strain redshifts the onset, while tensile strain blueshifts it. This behavior is consistently reflected in the dielectric function, refractive index, extinction coefficient, and optical conductivity. The energy loss function reveals a strain-dependent plasmon peak near 5 eV, further affirming the tunability of its electrodynamic response.

In summary, $Ca_3PBr_3$ emerges as an environmentally benign, mechanically stable, and strain-responsive semiconductor suitable for next-generation optoelectronic applications. Its direct and tunable bandgap, strong visible absorption, and flexibility-compatible mechanical profile make it a compelling candidate for strain-engineered devices such as flexible photovoltaics, tunable LEDs, and adaptive photodetectors. This work provides a foundational understanding of strain-mediated property modulation in lead-free perovskites and supports the ongoing search for sustainable high-performance materials.

**Conflict of Interest:** The authors declare no conflict of interest.

## References

1. Teo, S.H., Ng, C. H., Ng, Y. H., et al. “Resolve deep-rooted challenges of halide perovskite for sustainable energy development and environmental remediation”, *Nano Energy*, **99**, p. 107401 (2022). https://doi.org/10.1016/j.nanoen.2022.107401
2. Seyisi, T., Fouda-Mbanga, B. G., Mnyango, J. I., et al. “Major challenges for commercialization of perovskite solar cells: A critical review, *Energy Reports*, **13**, pp. 1400-1415 (2025). https://doi.org/10.1016/j.egyr.2025.01.019
3. Green, M. A., Ho-Baillie, A., and Snaith, H. J. “The emergence of perovskite solar cells”, *Nature photonics*, **8**(7), pp. 506-514 (2014). https://doi.org/10.1038/nphoton.2014.134
4. Correa-Baena, J. P., Saliba, M., Buonassisi, T., et al. “Promises and challenges of perovskite solar cells”, *Science*, **358**(6364), pp. 739-744 (2017). https://doi.org/10.1126/science.aam6323
5. Alsuhaibani, A. M., Kamran, M., Rehman, F., et al. “First-principle insight into structural, electronic, optical and elastic properties of AgXF3 (Cr, Zr) halide perovskite materials for application of reflective coating”, *Journal of Inorganic and Organometallic Polymers and Materials*, **34**(8), pp. 3613-3622 (2024). https://doi.org/10.1007/s10904-024-03035-1
6. Lin, H., Yang, M., Ru, X., et al. “Silicon heterojunction solar cells with up to 26.81% efficiency achieved by electrically optimized nanocrystalline-silicon hole contact layers”, *Nature Energy*, **8**(8), pp. 789-799 (2023). https://doi.org/10.1038/s41560-023-01255-2

7. Han, J., Park, K., Tan, S., et al. “Perovskite solar cells”, *Nature Reviews Methods Primers*, **5**(1), pp. 3 (2025). https://doi.org/s435-024-00373-9
8. Filip, M. R., Eperon, G. E., Snaith, H. J., et al.“ Steric engineering of metal-halide perovskites with tunable optical band gaps”, Nature communications, **5**(1), pp. 5757 (2014). https://doi.org/10.1038/ncomms6757
9. Ji, F., Klarbring, J., Wang, F., et al. “Lead‐free halide double perovskite Cs2AgBiBr6 with decreased band gap”, *Angewandte Chemie*, **132**(35), pp. 15303-15306 (2020). https://doi.org/10.1002/anie.202005568
10. Wang, Y., Liu, J., Liu, Y., et al. “Recent advances in lead-free halide perovskites: from synthesis to applications”, *Journal of Materials Chemistry C*, **12**(28): pp. 10267-10329 (2024). https://doi.org/10.1039/D4TC01556H
11. Riaz, M., Mukhtar, M. W., Ali, S. M., et al. “HSE03 functional-based DFT screening the multifaceted properties of inorganic halide perovskites ABI3 (a= ca, Ba; BK, Rb) for cutting-edge optoelectronic applications”, *Chemical Physics*, pp. 112881 (2025). https://doi.org/10.1016/j.chemphys.2025.112881
12. Rahman, M. H., Full, H., Rahman, M. A., et al. “ETL engineering in lead-free new Ca 3 PBr 3 perovskite type structure of anti-perovskite derivative material for stable and effective photovoltaic solar cells”, *New Journal of Chemistry*, **49**(8), pp. 3044-3066 (2025). https://doi.org/10.1039/d4nj03622k
13. Malan, C., K.K. Mishra, and R. Sharma, “Unveiling the potential of $Ca_3PBr_3$ perovskite for solar applications: A study of structural, mechanical, electronic and optical properties”, *Optik*, **327**, pp. 172310 (2025). https://doi.org/10.1016/j.ijleo.2025.172310
14. Ghosh, A., Ahmed, F., Ferdous, M. J., et al. “Strain-induced changes in the electronic, optical and mechanical properties of the inorganic cubic halide perovskite Sr3PBr3 with FP-DFT”, *Journal of Physics and Chemistry of Solids*, **191**, pp. 112053 (2024). https://doi.org/10.1016/j.jpcs.2024.112053
15. Zhu, C., Niu, X., Fu, Y., et al. “Strain engineering in perovskite solar cells and its impacts on carrier dynamics”, *Nature communications*, **10**(1), pp. 815 (2019). https://doi.org/10.1038/s41467-019-08507-4
16. Yang, J., P. Manganaris, and A. Mannodi-Kanakkithodi, “A high-throughput computational dataset of halide perovskite alloys”, *Digital Discovery*, **2**(3), pp. 856-870 (2023). https://doi.org/10.1039/D3DD00015J
17. Islam, R., Liu, K., Wang, Z., et al. “Strain-induced electronic and optical properties of inorganic lead halide perovskites APbBr3 (A= Rb and Cs)”, *Materials Today Communications*, **31**, pp. 103305 (2022). https://doi.org/10.1016/j.mtcomm.2022.103305
18. Even, J., Pedesseau, L., Jancu, J. M., et al. “Importance of spin–orbit coupling in hybrid organic/inorganic perovskites for photovoltaic applications”, *The Journal of Physical Chemistry Letters*, **4**(17), pp. 2999-3005 (2013). https://doi.org/10.1021/jz401532q
19. Mouhat, F. and F.-X. Coudert, “Necessary and sufficient elastic stability conditions in various crystal systems”, *PhysRevB*, **90**(22), pp. 224104(2014). https://doi.org/10.1103/PhysRevB.90.224104
20. Smidstrup, S., Markussen, T., Vancraeyveld, P., et al. “QuantumATK: an integrated platform of electronic and atomic-scale modelling tools”, *Journal of Physics: Condensed Matter*, **32**(1), pp. 015901 (2019). https://doi.org/10.1088/1361-648X/ab4007
21. Tang, T., and Tang, Y. “First-principles calculations of orthorhombic chalcogenide ABX3 (A= Ca, Sr, Ba; B= Ge, Sn; X= O, S, Se, Te) perovskites by cation and anion variation”, *Inorganic Chemistry Communications*, **171**: pp. 113461 (2025). https://doi.org/10.1016/j.inoche.2024.113461
22. Nocedal, J. “Updating quasi-Newton matrices with limited storage”, *Mathematics of computation*, **35**(151), pp. 773-782 (1980). https://doi.org/10.2307/2006193
23. Perdew, J.P., K. Burke, and M. Ernzerhof. “Generalized gradient approximation made simple”, *Physical review letters*, **77**(18), pp. 3865 (1996). https://doi.org/10.1103/PhysRevLett.77.3865
24. Heyd, J., G.E. Scuseria, and M. Ernzerhof. “Hybrid functionals based on a screened Coulomb potential”, *The Journal of chemical physics*, **118**(18), pp. 8207-8215 (2003). https://doi.org/10.1063/1.1564060
25. Hummer, K., J. Harl, and G. Kresse. “Heyd-Scuseria-Ernzerhof hybrid functional for calculating the lattice dynamics of semiconductors”, *Physical Review B—Condensed Matter and Materials Physics*, **80**(11), pp. 115205 (2009). https://doi.org/10.1103/PhysRevB.80.115205
26. Monkhorst, H.J., and J.D. Pack. “Special points for Brillouin-zone integrations”, *Physical review B*, **13**(12), pp. 5188 (1976). https://doi.org/10.1103/PhysRevB.13.5188
27. Shockley, W. and H. Queisser, “Detailed balance limit of efficiency of p–n junction solar cells”, *in Renewable energy*, Routledge. pp. Vol2_35-Vol2_54 (2018). https://doi.org/10.1063/1.1736034
28. Algahtani, A., Rehman, F., Liaqat, M., et al. “Probing the physical properties of Sr3AsX3 (X= F and Br) perovskite compounds for prospective solar cell applications employing the DFT framework”, *Inorganic Chemistry Communications*, **162**, pp. 112186 (2024). https://doi.org/10.1016/j.inoche.2024.112186

29. Zheng, F., Tan, L. Z., Liu, S., et al. "Rashba spin–orbit coupling enhanced carrier lifetime in CH3NH3PbI3", *Nano letters*, **15**(12), pp. 7794-7800 (2015). https:// doi.org/10.1021/acs.nanolett.5b01854

## Biography

## Author:

**Fatemeh Nemati:** Fatemeh Nemati received her Ph.D. degree in Elementry Particle Physics and Field Theory in from Urmia University of Technology, Iran. She is currently working on first-principles simulations of lead-free halide perovskites inored to use in solar cells. At the same times, she work on a team to design a single-photon source. In addition, she assists as an thesis adviser.

**Reza Habibpourbisafar:** Reza Habibpourbisafar received his M.Sc. degree in Physics from Urmia University of Technology, Iran. Also he is currently pursuing his Ph.D. in condensed matter physics in University of Tabriz. His research focuses on first-principles simulations of lead-free halide perovskites, including their electronic, optical, and mechanical properties under strain. he has extensive experience using density functional theory methods and computational tools such as QuantumATK and VASP. His work aims to understand and design novel perovskite materials for potential applications in optoelectronic device.

**Elaheh Javanshoor:** Elaheh Javanshoor received her Ph.D. degree in Elementry Particle Physics and Field Theory in from Urmia University of Technology, Iran. She is currently working on designing the biosensor based novel materials.

## Figure Caption

Figure.1, Cubic perovskite structure of $Ca_3PBr_3$.

Figure.2, Energy volume curve of $Ca_3PBr_3$ for strain from -4% to 4%.

Figure.3, Electronic band structure of $Ca_3PBr_3$ without strain. (a) Calculations using GGA-PBE (red) and hybrid HSE06 (blue) exchange-correlation functions show a direct bandgap at the Brillouin zone center. (b) A comparison between the non-spin-polarized GGA-PBE (red) and spin-polarized calculations including spin-orbit-coupling (SO) GGA-PBE (green) illustrates the effect of SOC on the band-edge positions. The results confirm the semiconducting nature and direct gap of the material.

Figure.4, Strain-dependent electronic band structures of $Ca_3PBr_3$ under various biaxial strain levels, calculated using both non-spin-polarized GGA-PBE and spin-polarized including spin-orbit coupling (SOC) GGA-PBE. Panels show (a) -4% strain, (b) -2% strain, (c) +2% strain, and (d) +4% strain. The band edges shift systematically in response to compressive and tensile deformation.

Figure.5, Strain-dependent projected density of states of $Ca_3PBr_3$ under biaxial strains of –4%, -2%, 0%, 2%, +4%. Each strain condition is shown for both GGA-PBE (left panels), HybridGGA-HSE06 (center panel) and SOGGA-PBE exchange-correlation functionals. (right panels). Across all cases, the valence band is dominated by Br-4p states purple) and P-3p states (deep blue), while the conduction band is primarily composed of Ca-3d states (cyan). Strain modifies the band edges, with compressive strain narrowing the bandgap and tensile strain widening it, while the orbital character remains unchanged.

Figure.6, Real *($\varepsilon_1$)* and imaginary *($\varepsilon_2$)* parts of the dielectric function under biaxial strain (–4% to +4%). The absorption onset in $\varepsilon_2(\omega)$ shifts with the fundamental bandgap.

Figure.7, Energy loss function $L(\omega)$, calculated from $\varepsilon(\omega)$, showing a strain-tunable plasmon peak near 5 eV.

Figure.8, Key optical coefficients under strain: absorption, reflectivity, extinction coefficient, and refractive index. All exhibit the consistent strain-dependent shifts established by the dielectric function.

Figure.9, Optical conductivity $\sigma(\omega)$ showing strain-tunable interband transitions.

## Table Caption

Table.1, Optimized lattice constants of $Ca_3PBr_3$ obtained in this work compared with previously reported theoretical and experimental values.

Table.2, The calculated values of elestic constants $C_{ij}$ *(GPa)*, Cauchy pressure $C_{12}–C_{44}$ *(GPa)*, Pugh ratio (*B/G*), and Poisson's ratio ($\nu$) of cubic $Ca_3PBr_3$ perovskite under different strain values at Using GGA-PBE pseudopotential basis (first raw)/ Using SOGGA-PBE exchange-correlation functional. (second raw) state.

Table.3, Calculated band gaps ($E_g$) of $Ca_3PBr_3$ without strain and with biaxial strain conditions using GGA-PBE and HSE06 functionals, with and without spin-orbit coupling (SOC). All band gaps are in eV.

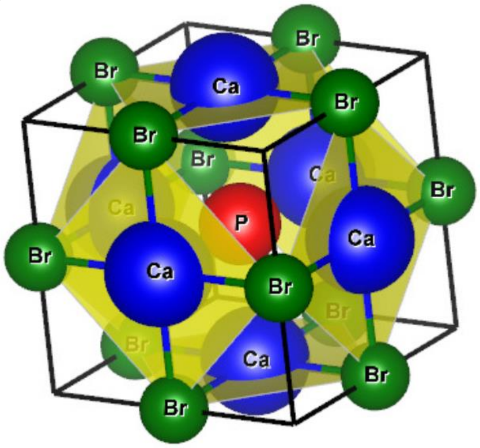

***Figure 1.***

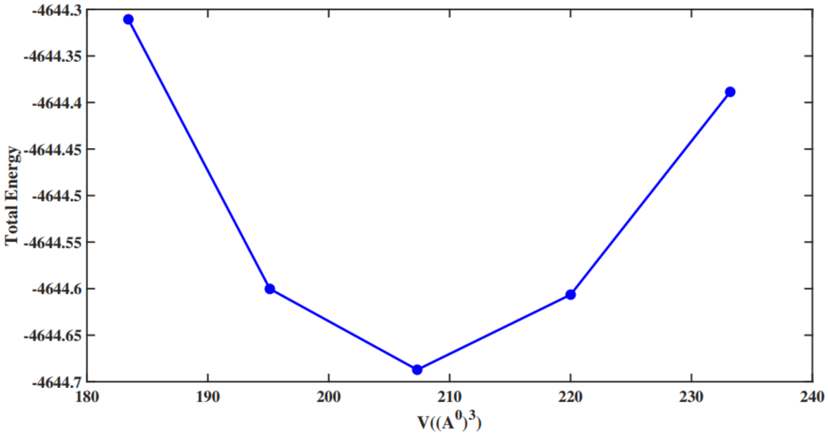

*Figure 2.*

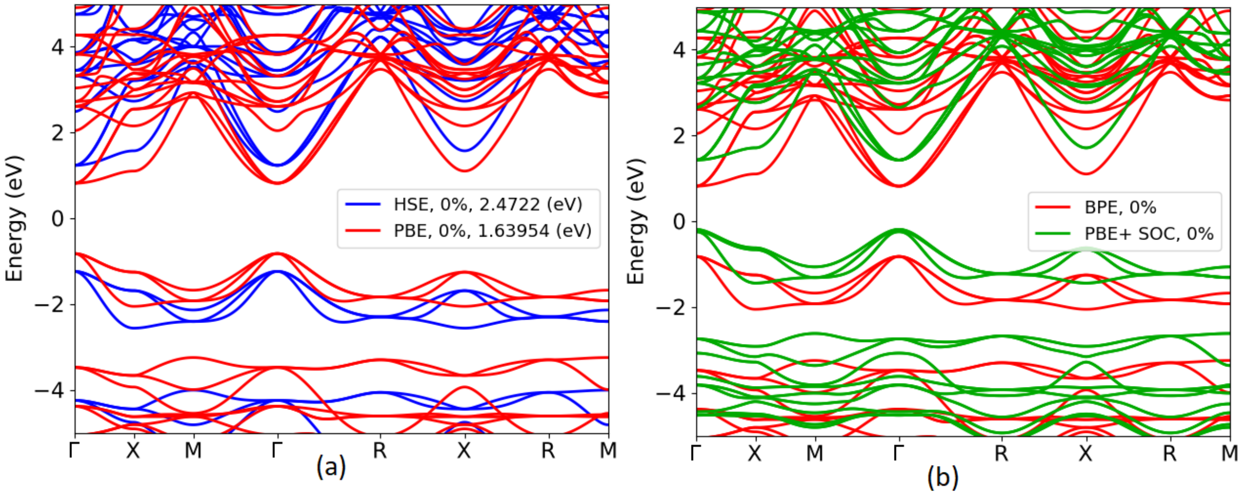

(a)

(b)

*Figure 3.*

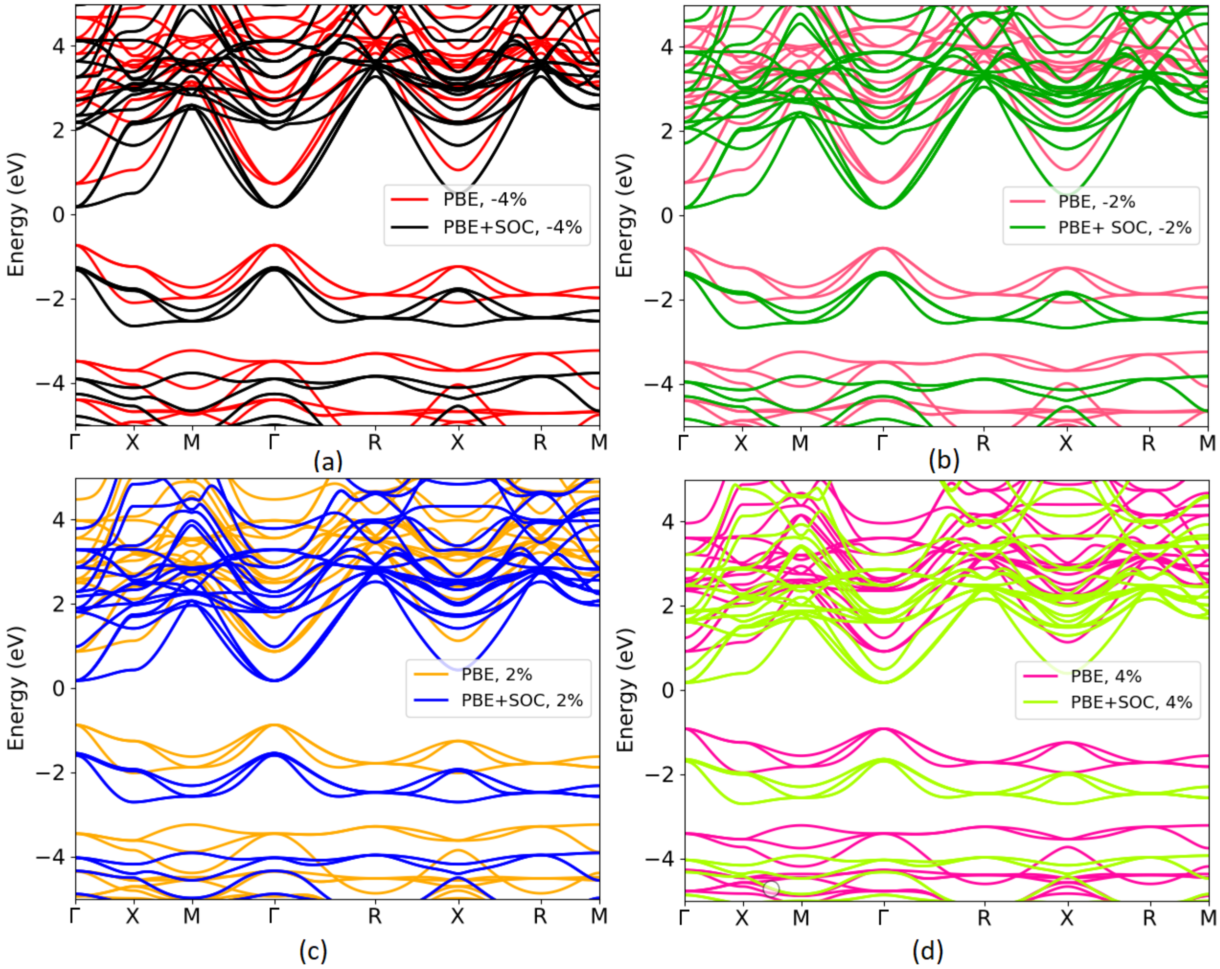

(a) (b)

(c) (d)

***Figure 4.***

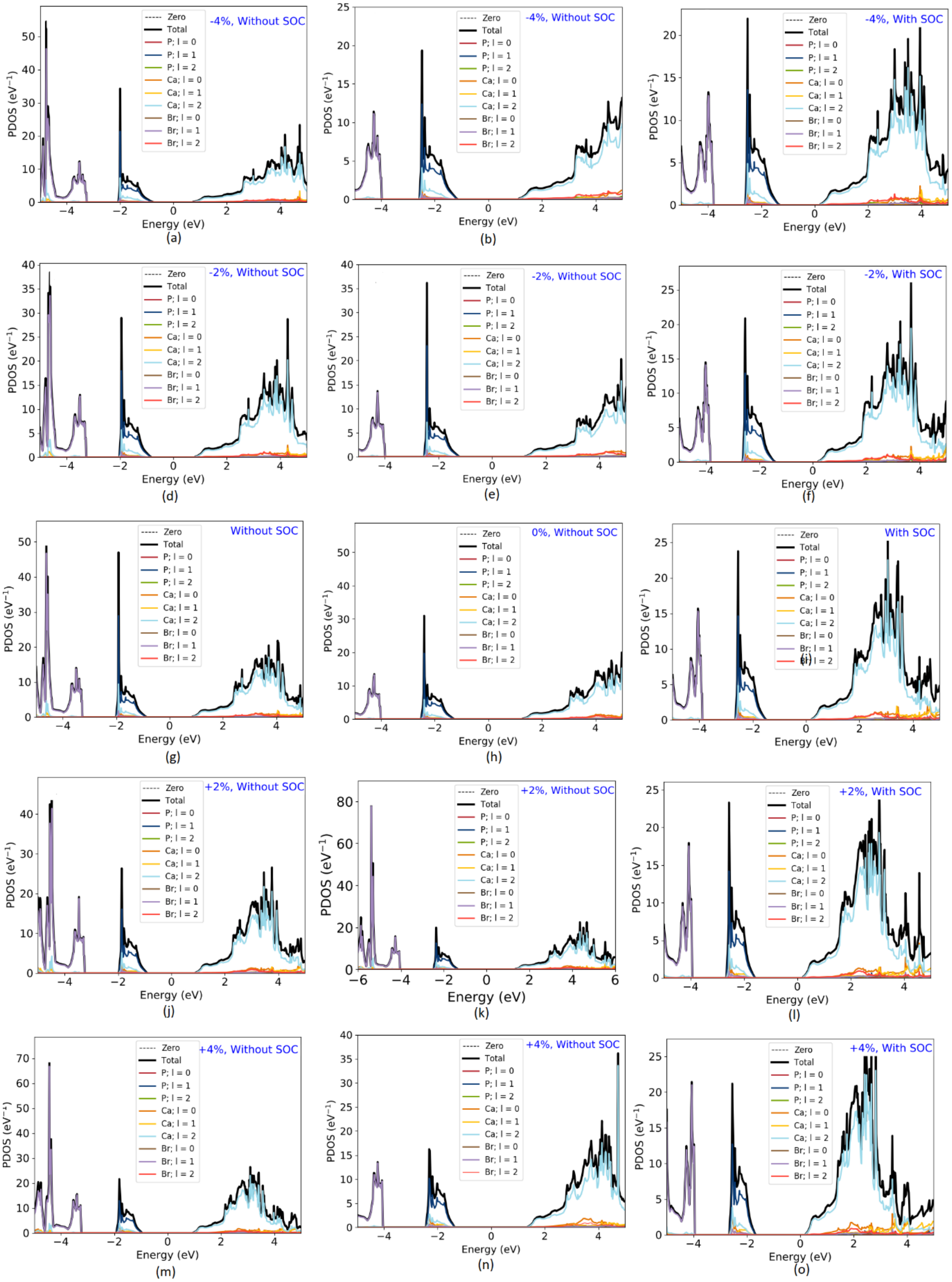-4%, Without SOC
-4%, Without SOC
-4%, With SOC
-2%, Without SOC
-2%, Without SOC
-2%, With SOC
Without SOC
0%, Without SOC
With SOC
+2%, Without SOC
+2%, Without SOC
+2%, With SOC
+4%, Without SOC
+4%, Without SOC
+4%, With SOC
Zero
Total
P; l = 0
P; l = 1
P; l = 2
Ca; l = 0
Ca; l = 1
Ca; l = 2
Br; l = 0
Br; l = 1
Br; l = 2
PDOS (eV$^{-1}$)
Energy (eV)
(a)
(b)
(c)
(d)
(e)
(f)
(g)
(h)
(i)
(j)
(k)
(l)
(m)
(n)
(o)

*Figure 5*

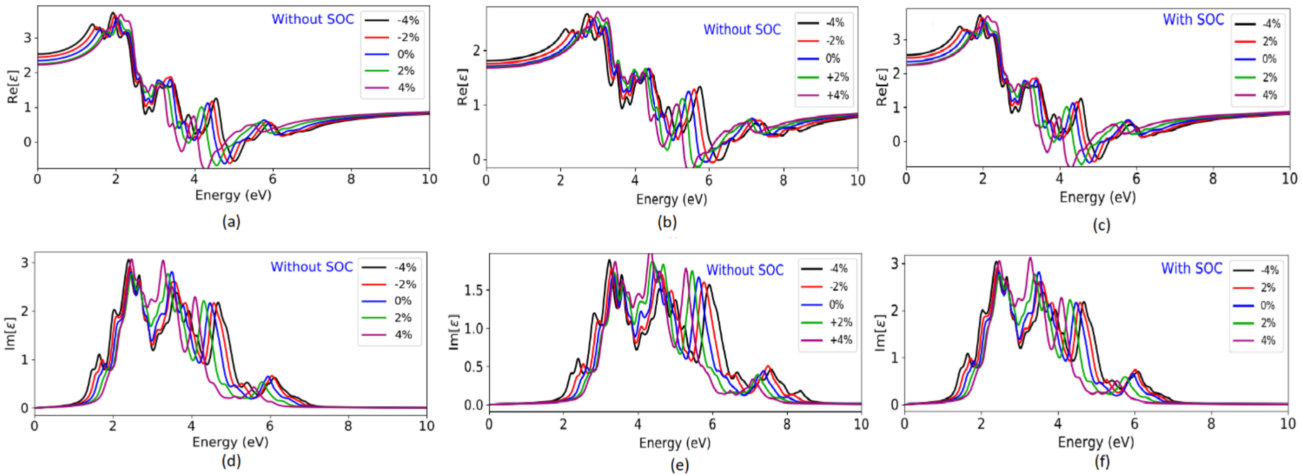

*Figure 6*.

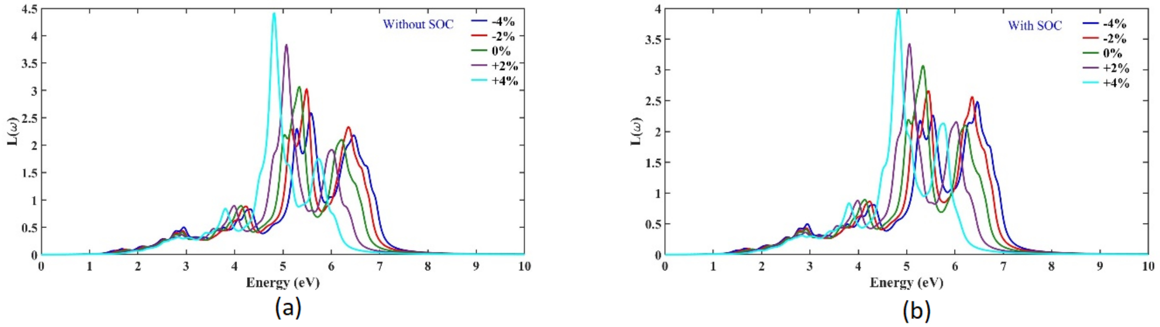

*Figure 7.*

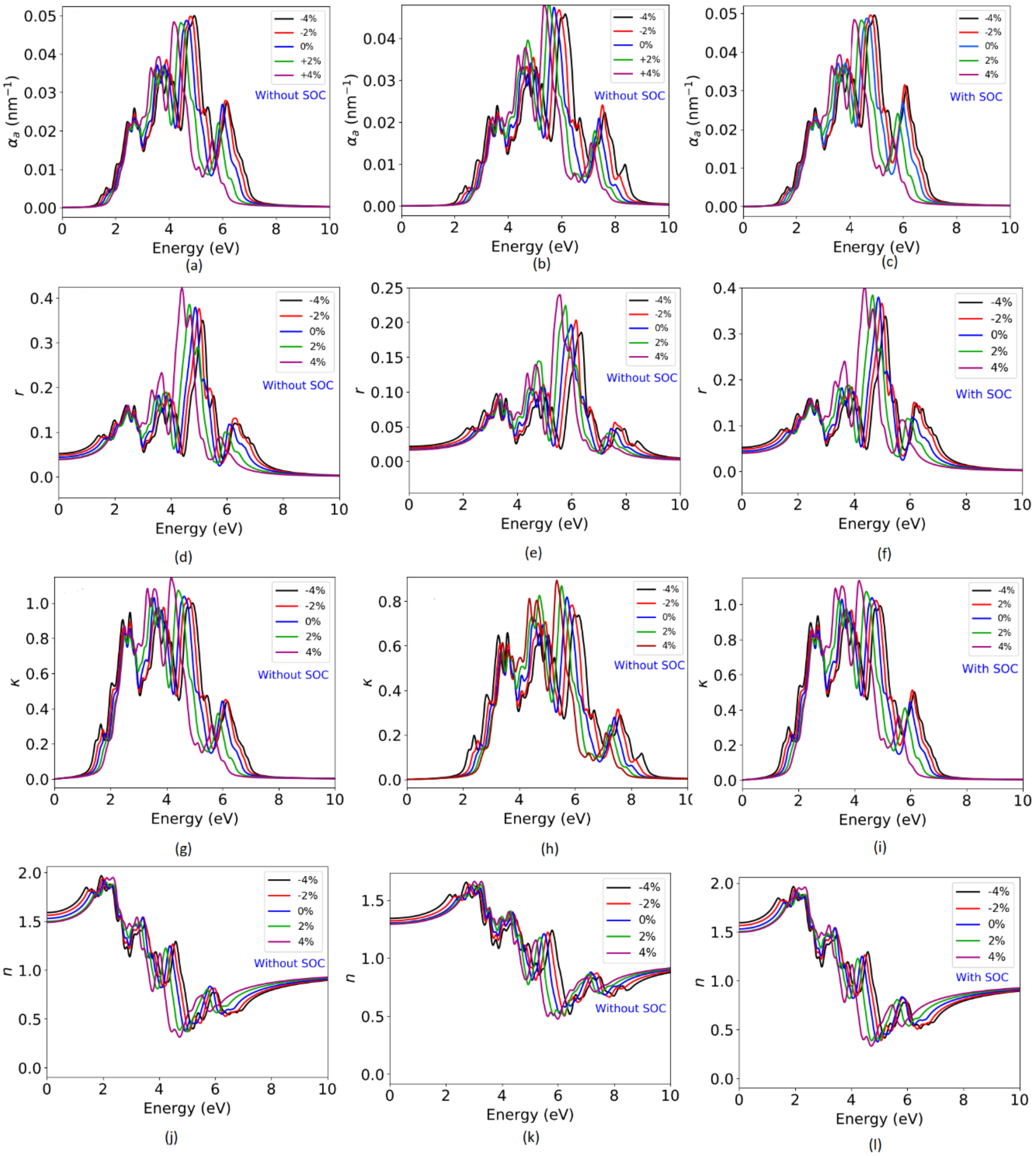
$\alpha_a$ (nm$^{-1}$)
r
κ
n
Energy (eV)
-4%
-2%
0%
+2%
+4%
2%
4%
Without SOC
With SOC
(a)
(b)
(c)
(d)
(e)
(f)
(g)
(h)
(i)
(j)
(k)
(l)

***Figure 8***.

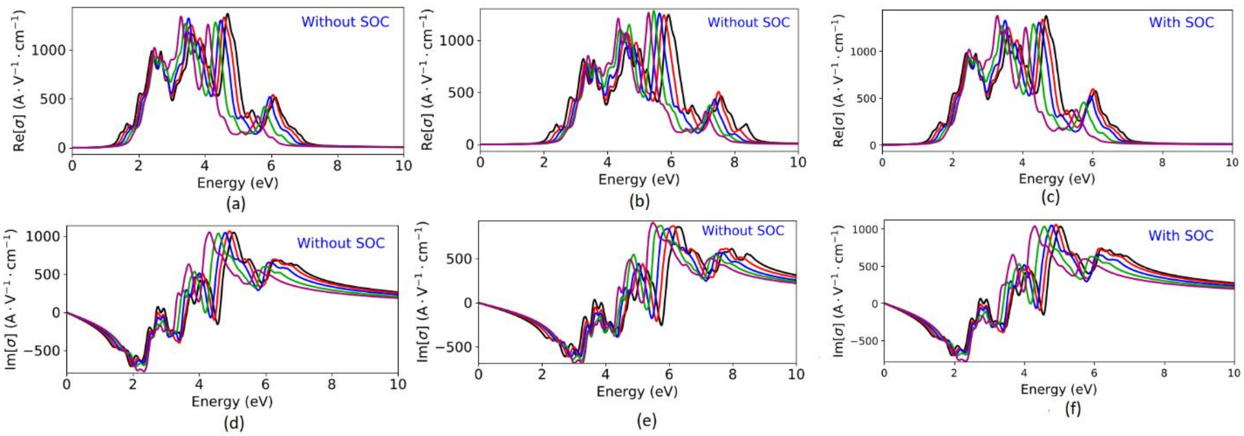

***Figure 9.***

***Table 1.***

| Reference | Method | a(Å) |
|---|---|---|
| This work | DFT (GGA-PBE) | 5.9185 |
| Rahman *et al.* | DFT (GGA-PBE) | 6.48 |
| Malan *et al.* | DFT (GGA-PBE) | 6.47 |
| Riaz *et al.* | DFT (HSE06) | 6.42 |

***Table 2.***

| Strain(%) | $C_{11}$ | $C_{12}$ | $C_{44}$ | $C_{12}$-$C_{44}$ | *B/G* | *v* |
|---|---|---|---|---|---|---|
| -4 | 128.76 | 13.05 | 23.38 | -10.39 | 1.68 | 0.24 |
| | 128.76 | 12.96 | 23.35 | -10.39 | 1.68 | 0.24 |
| -2 | 105.04 | 12.21 | 20.88 | -8.67 | 1.61 | 0.23 |
| | 104.89 | 12.24 | 20.86 | -8.62 | 1.61 | 0.23 |
| 0 | 85.18 | 12.51 | 18.76 | -6.25 | 1.58 | 0.23 |
| | 85.28 | 12.48 | 18.76 | -6.28 | 1.58 | 0.23 |
| +2 | 60.57 | 11.64 | 16.03 | -4.39 | 1.50 | 0.21 |
| | 60.63 | 11.62 | 16.02 | -4.40 | 1.50 | 0.21 |
| +4 | 33.01 | 11.74 | 13.06 | -1.32 | 1.57 | 0.22 |
| | 37.09 | 10.56 | 13.06 | -2.50 | 1.48 | 0.21 |

***Table 3.***

| Strain(%) | PBE | PBE-SOC | HSE06 |
|---|---|---|---|
| -4 | 1.4604 | 1.4372 | 2.19176 |
| -2 | 1.55 | 1.53 | 2.3506 |
| 0 | 1.6395 | 1.6173 | 2.4722 |
| +2 | 1.74 | 1.72 | 2.56464 |
| +4 | 1.8366 | 1.8176 | 2.66485 |
| Rahman *et al.* | 1.65 | - | 2.63 |
| Malan *et al.* | 1.682 | - | - |